Science Arts & Métiers (SAM)

is an open access repository that collects the work of Arts et Métiers Institute of Technology researchers and makes it freely available over the web where possible.

This is an author-deposited version published in: https://sam.ensam.eu
Handle ID: .http://hdl.handle.net/10985/19895

To cite this version :

Qiang CHEN, Wenqiong TU, Meng MA - Deep learning in heterogeneous materials: Targeting the thermo-mechanical response of unidirectional composites - Journal of Applied Physics - Vol. 127, n°17, p.175101 - 2020

Any correspondence concerning this service should be sent to the repository Administrator : scienceouverte@ensam.eu

Arts et Métiers Institute of Technology

Deep learning in heterogeneous materials: Targeting the thermo-mechanical response of unidirectional composites

Qiang Chen,[1] Wenqiong Tu,[2] and Meng Ma[3,a)]

AFFILIATIONS

[1]LEM3-UMR 7239 CNRS, Arts et Métiers ParisTech Metz, 4 Rue Augustin Fresnel, Metz 57078, France
[2]Engineering Technology Associates, Inc., 1133 E Maple Rd., Troy, Michigan 48083, USA
[3]Department of Mechanical Engineering, University of Massachusetts Lowell, 1 University Avenue, Lowell, Massachusetts 01854, USA

Note: This paper is part of the special collection on Machine Learning for Materials Design and Discovery
[a)]**Author to whom correspondence should be addressed:** Meng_Ma@uml.edu

ABSTRACT

In this communication, a multi-task deep learning-driven homogenization scheme is proposed for predicting the effective thermomechanical response of unidirectional composites consisting of a random array of inhomogeneity. Toward this end, 40 000 repeating unit cells (RUCs) comprising an arbitrary number of locally irregular inclusions are generated over a wide range of fiber volume fractions. The finite-volume direct averaging micromechanics is then employed to evaluate the homogenized thermo-mechanical moduli of each RUC. Subsequently, a two-dimensional deep convolution neural network (CNN) is constructed as a surrogate model to extract the statistical correlations between the RUC geometrical information and the corresponding homogenized response. The RUC images together with their homogenized moduli are divided into two datasets in a ratio of 9:1 with the former part used for training the CNN model and the latter part used for verification. The results presented in this contribution demonstrate that the deep CNN predictions exhibit remarkable correlations with the theoretical values generated by the finite-volume micromechanics, with a maximum relative prediction error of less than 8%, providing good support for the data-based homogenization approach.

I. INTRODUCTION

Heterogeneous materials possess unique thermo-mechanical and physical properties for specific applications in emerging technologies. Due to the myriad combinations of both geometric configurations and constituent materials that may be realized in the modern heterogeneous material system, micromechanics-based simulation of the thermo-mechanical response of composites continues to play a significant role in the development and design of novel materials and structures with superior properties.[1–3] At the fundamental level, micromechanics facilitates the analysis, design, and optimization of heterogeneous materials and structures with different microstructural architectures and scales, along with the understanding of the underlying theoretical issues and underpinning multi-physics mechanisms.

A large body of work already exists aimed at the micromechanical modeling of the thermo-mechanical and multiphysics behavior of heterogeneous materials, ranging from the simplest rule-of-mixture assumptions and processing to the more complex geometric models that require computationally demanding analytical and numerical treatment.[4–7] In general, these approaches can be categorized into two broad categories, namely, the representative volume element (RVE) and repeating unit cell (RUC) based approaches, according to the different geometric representations of material microstructures that involve the concepts of statistical homogeneity and periodicity,[8,9] respectively. The extensively employed composite cylinder and sphere assemblage models,[10] the Mori–Tanaka scheme,[11] and the three-phase model[4] were the earliest and most classic geometric RVE-based models that provide explicit expressions for the effective moduli. Nonetheless, those approaches neglect the actual microstructural details of heterogeneous materials and hence do not take into account the interaction of adjacent inclusions. At large volume

fractions, the interaction of the adjacent inclusions is significant and its neglect may significantly underestimate the local stress fields that affect the effective moduli and, more importantly, the failure strength.

The alternative approaches that generate accurate homogenized and localized response for composites with complex microstructures are the RUC-based approaches that explicitly impose periodic boundary conditions, such as finite-element (FE)-based variational techniques[12,13] or the elasticity-based locally exact homogenization theory (LEHT).[14] However, the FE approaches require substantial computational effort and hence may not be easily employed in parametric studies, whereas the LEHT is presently limited to continuous fibers with circular cross sections let alone the fact that the implementations are very difficult for nonprofessional users. The finite-volume (FV) direct averaging homogenization approach for periodic composites materials, Gattu *et al.*[15] and Chen *et al.*,[16] provides a viable alternative to the finite-element or locally exact homogenization techniques. The FV micromechanics predicts undistinguishable localized and effective response relative to the FE and LEHT techniques but offers a large number of advantages perfectly suited for parametric studies, including the availability of closed-form expressions for the local stiffness matrices, substantially less execution time, excellent numerical stabilities and convergence behaviors, and the ability to simulate complex microstructures. A fundamental difference between the finite-volume- and finite-element-based solutions of the unit cell problem is the manner of satisfying local, and thus global, equilibrium equations. While the minimization of total potential energy within the finite-element framework leads to ultimate satisfaction of the unit cell's global equilibrium with sufficient mesh refinement, the finite-volume approach enforces equilibrium in the integral sense for every subvolume at each level of mesh refinement. The readers are referred to recent review articles by Chen and Pindera[17] and Chen *et al.*[18] for additional references in this area.

Despite rapid advances in micromechanics and homogenization theories, interest in developing accurate yet efficient surrogate models based on big data analysis has also attracted growing attention.[19–22] The deep learning methods enable the progressive extraction of higher-level features from the raw data, which have gained tremendous applications in processing images, video, speech, and audio.[23–25] Their successful applications motivate us to develop a data-based homogenization technique to predict the homogenized thermo-mechanical response of heterogeneous materials.

Herein, we propose a deep convolution neural network (CNN)-driven homogenization scheme to investigate the variation of thermo-mechanical moduli of unidirectional composites with complex microstructures. The finite-volume direct averaging micromechanics is employed to generate the input layer used in the deep convolution neural network. It should be noted that 40 000 sets of homogenized moduli for multi-inclusion unit cells were generated using the finite-volume homogenization technique in an uncompiled MATLAB environment, which may not be easily achieved in the case of the primal finite-element calculations. Two material systems that are widely used in aerospace and wind energy engineering, namely, graphite/epoxy and glass/epoxy composites, which yield different fiber/matrix modulus ratios, are considered. After training with 36 000 sets of homogenized moduli for multi-inclusion unit cells generated via the finite-volume homogenization technique, the deep CNN can directly map the structural information of heterogeneous materials onto their homogenized thermomechanical properties without the need for solving the RUC problems via either analytical or numerical approaches. Hence, with the trained deep CNN, a researcher untrained in the techniques of homogenization would be able to obtain homogenized moduli of periodic composites with locally random reinforcement distribution by using this algorithm upon securing an image of the material's microstructural features. Section II describes the theoretical framework that combines the finite-volume micromechanics and deep convolution neural network. Section III presents two numerical examples to validate the data-driven homogenization scheme. Section IV concludes the present contribution.

II. THEORETICAL FRAMEWORK

A. Finite-volume direct averaging micromechanics

The finite-volume direct averaging micromechanics is capable of rapidly generating a full set of effective thermo-mechanical moduli for composites whose microstructures are distributed periodically in the space; hence, it is used to construct the input dataset for the deep CNN algorithm. Herein, only essential information necessary to understand how it is implemented into CNN is presented, while details of the finite-volume homogenization theory can be found in Refs. 15 and 16.

The finite-volume micromechanics is based on the microstructural discretization of a repeating unit cell into hexahedral (or quadrilateral) subvolumes designated by the index q. The central problem of the finite-volume-based micromechanical analysis of composite materials becomes the determination of strain concentration tensors $\mathbf{A}^{(q)}$ relating the average strains $\bar{\boldsymbol{\varepsilon}}^{(q)}$ in the qth phase to the applied strains $\bar{\boldsymbol{\varepsilon}}$. In the presence of thermal effects represented by the vector $\mathbf{D}^{(q)}$, the localization relation takes the form

$$\bar{\boldsymbol{\varepsilon}}^{(q)} = \mathbf{A}^{(q)}\bar{\boldsymbol{\varepsilon}} + \mathbf{D}^{(q)}, \tag{1}$$

where $\mathbf{A}^{(q)}$ is elastic strain concentration matrix. Application of one non-zero macroscopic strain component in the absence of temperature variation determines one column vector of $\mathbf{A}^{(q)}$, which is done just once. In addition, $\mathbf{D}^{(q)} = \bar{\boldsymbol{\varepsilon}}^{(q)} - \mathbf{A}^{(q)}\bar{\boldsymbol{\varepsilon}}$ can be interpreted as the thermal influence function. The use of localization relations in the average composite stress definition, in conjunction with the volume-averaged stress–strain relations for each phase, yields the homogenized constitutive equation for a multiphase composite,

$$\bar{\boldsymbol{\sigma}} = \frac{1}{V}\int_V \boldsymbol{\sigma}(x)\mathrm{d}V = \sum_{q=1}^{N_q} v_{(q)}\bar{\boldsymbol{\sigma}}^{(q)} = \mathbf{C}^*(\bar{\boldsymbol{\varepsilon}} - \bar{\boldsymbol{\varepsilon}}^{th}), \tag{2}$$

where $v_{(q)} = V^{(q)}/V$ is the volume fraction of the qth phase. The homogenized stiffness matrix $\mathbf{C}^*$ and the thermal strains $\bar{\boldsymbol{\varepsilon}}^{th}$ are given in terms of the subvolume geometry, material properties,

elastic concentration matrices, and their thermal counterparts,

$$\begin{aligned}\mathbf{C}^{*} &= \sum_{q=1}^{N_q} v_{(q)}\mathbf{C}^{(q)}\mathbf{A}^{(q)},\\ \bar{\boldsymbol{\varepsilon}}^{th} &= -[\mathbf{C}^{*}]^{-1}\sum_{q=1}^{N_q} v_{(q)}\mathbf{C}^{(q)}[\mathbf{D}^{(q)} - \boldsymbol{\alpha}^{(q)}\triangle T],\end{aligned} \tag{3}$$

where $\boldsymbol{\alpha}^{(q)}$ is the thermal expansion vector, $\mathbf{C}^{(q)}$ denotes the elastic stiffness matrix of the *qth* subvolume, and $\triangle T$ represents the temperature variation, which is assumed to be uniform throughout the repeating unit cell. The homogenized thermal expansion coefficients can be readily obtained according to

$$\boldsymbol{\alpha}^{*} = \bar{\boldsymbol{\varepsilon}}^{th}/\Delta T = [\mathbf{C}^{*}]^{-1}\sum_{q=1}^{N_q} v_{(q)}\mathbf{C}^{(q)}[\boldsymbol{\alpha}^{(q)} - \mathbf{D}^{(q)}/\triangle T]. \tag{4}$$

In the present work, we limit our analysis to unidirectional composites with continuous reinforcements whose response may be characterized by repeating material microstructures with two-dimensional periodicity. Following the zeroth-order homogenization theory,[8,26] the displacement field in the qth subvolume is expressed in terms of two-scale expansion involving macroscopic displacement $\bar{\varepsilon}_{ij}x_j$ and microstructure-induced fluctuating displacement $u_i'^{(q)}(y)$ as follows:

$$u_i^{(q)}(\mathbf{x}, \mathbf{y}) = \bar{\varepsilon}_{ij}x_j + u_i'^{(q)}(\mathbf{y}), \tag{5}$$

where $\mathbf{x} = (x_1, x_2, x_3)$ and $\mathbf{y} = (y_2, y_3)$ are the global and local coordinates, respectively, and $\bar{\varepsilon}_{ij}$ are the macroscopic (or applied) strains. $u_i'^{(q)}(y)$ that are periodic functions in the RUC coordinates are the fluctuating displacements,

$$\begin{aligned}u_i'^{(q)}(\mathbf{y}(\eta,\xi)) = {} & W_{i(00)}^{(q)} + \eta W_{i(10)}^{(q)} + \xi W_{i(01)}^{(q)} + \frac{1}{2}(3\eta^2 - 1)W_{i(20)}^{(q)}\\ & + \frac{1}{2}(3\xi^2 - 1)W_{i(02)}^{(q)},\end{aligned} \tag{6}$$

which produce local strains in the form:

$$\boldsymbol{\varepsilon}_{ij}^{(q)} = \bar{\boldsymbol{\varepsilon}}_{ij} + \boldsymbol{\varepsilon}_{ij}'^{(q)} = \bar{\boldsymbol{\varepsilon}}_{ij} + \frac{1}{2}\left(\frac{\partial u_i'^{(q)}}{\partial y_j} + \frac{\partial u_j'^{(q)}}{\partial y_i}\right), \tag{7}$$

where $\boldsymbol{\varepsilon}_{ij}'^{(q)}$ are the strain fluctuations induced by microstructures. $W_{i(..)}^{(q)}$ are the unknown coefficients in the displacement field representation. Those coefficients are expressed in terms of surface-averaged interfacial displacements $\hat{u}_i'^{(p,q)}$ upon the use of the definition of the surface-averaged interfacial displacements, Eq. (8), together with the application of equilibrium equation within each subvolume in the large, Eq. (9),

$$\hat{u}_i'^{(1,3)} = \frac{1}{2}\int_{-1}^{+1} u'_i(\eta, \mp 1)\mathrm{d}\eta \qquad \hat{u}_i'^{(2,4)} = \frac{1}{2}\int_{-1}^{+1} u'_i(\pm 1, \xi)\mathrm{d}\xi, \tag{8}$$

$$\int_{S_q}\boldsymbol{\sigma}^{(q)}\cdot\mathbf{n}^{(q)}dS = \int_{S_q}\mathbf{t}^{(q)}dS = \sum_{p=1}^{4}\int_{l_p^{(q)}}\mathbf{t}^{(p,q)}dl_p^{(q)} = \sum_{p=1}^{4} l_p^{(q)}\hat{\mathbf{t}}^{(p,q)} = 0, \tag{9}$$

where $l_p^{(q)}$ is the length of the pth face in the qth subvolume, $\mathbf{n}^{(q)}$ is unit vector that defines the orientation of each of the four subvolume faces, and $\mathbf{t}^{(p,q)} = \boldsymbol{\sigma}^{(p,q)}\cdot\mathbf{n}^{(p,q)}$ from Cauchy's relation. Evaluating the surface-averaged tractions in terms of the surface-averaged displacements yields the following system of equations:

$$\hat{\mathbf{t}}^{(q)} = \mathbf{k}^{(q)}\hat{\mathbf{u}}'^{(q)} + \mathbf{N}^{(q)}\mathbf{C}^{(q)}(\bar{\boldsymbol{\varepsilon}} - \boldsymbol{\alpha}^{(q)}\Delta T), \tag{10}$$

where $\hat{\mathbf{t}}^{(q)} = [\hat{\mathbf{t}}^{(1)}\,\hat{\mathbf{t}}^{(2)}\,\hat{\mathbf{t}}^{(3)}\,\hat{\mathbf{t}}^{(4)}]^{(q)\mathrm{T}}$ with $\hat{\mathbf{t}}^{(p)} = [t_1\ t_2\ t_3]^{(p)\mathrm{T}}$, $\hat{\mathbf{u}}'^{(q)} = [\hat{\mathbf{u}}'^{(1)}\,\hat{\mathbf{u}}'^{(2)}\,\hat{\mathbf{u}}'^{(3)}\,\hat{\mathbf{u}}'^{(4)}]^{(q)\mathrm{T}}$ with $\hat{\mathbf{u}}'^{(p)} = [\hat{u}'_1\,\hat{u}'_2\,\hat{u}'_3]^{(p)\mathrm{T}}$, and $\mathbf{N}^{(q)} = [\mathbf{n}^{(1)}\,\mathbf{n}^{(2)}\,\mathbf{n}^{(3)}\,\mathbf{n}^{(4)}]^{(q)\mathrm{T}}$. The local stiffness matrix $\mathbf{k}^{(q)}$ is comprised of 16 submatrices $\mathbf{k}_{ij}^{(q)}$ with the element of each 3×3 submatrix derived in closed form in terms of subvolume geometry and material properties, the expressions of which can be found in the Ref. 15.

The application of interfacial traction and displacement continuity conditions at common subvolume face, in conjunction with the periodic conditions at the mirror faces of the RUC, produces a global system of equations for the determination of interfacial displacements $\hat{\mathbf{U}}'$, which can be symbolically expressed in the following form:

$$\mathbf{K}\hat{\mathbf{U}}' = \mathbf{F}(\bar{\boldsymbol{\varepsilon}}, \Delta T), \tag{11}$$

where $\mathbf{K}$ denotes the assembled global stiffness matrix given explicitly in terms of subvolume geometry and material properties and $\mathbf{F}(\bar{\boldsymbol{\varepsilon}}, \Delta T)$ is the macroscopic loading vector. Once the interfacial surface-averaged displacements $\hat{\mathbf{U}}'$ are obtained, the subvolume strains and hence strain concentration matrices $\mathbf{A}^{(q)}$ and effective stiffness $\mathbf{C}^{*}$ will be readily determined.

B. Deep convolution neural network

Among the deep learning architectures, convolution neural networks are developed based on the idea of local connectivity of convolutional operation between two layers.[27] The convolution operation is achieved by passing a kernel through an input volume, which can be two or three dimensions. In this process, the matrix multiplication between the kernel and the corresponding part of the input that matches the same size is conducted and then the sum over the matrix is provided as the value of one cell of convolutional result, as shown in Fig. 1. The first orange shaded cell in the output volume is the convolution of upper left cells in the input volume with the kernel. Then the kernel will slide according to the input until it comes to the last point. The kernel (also called the filter) is convolved with the input to create a feature map, which shares the same weights for the convolution, reducing the total number of learnable parameters.[28] For a convolutional layer, the convolution is performed on the feature map of the previous layer with learnable kernels. Then the current feature map is obtained by using the activation function at the activation layer. In general, for

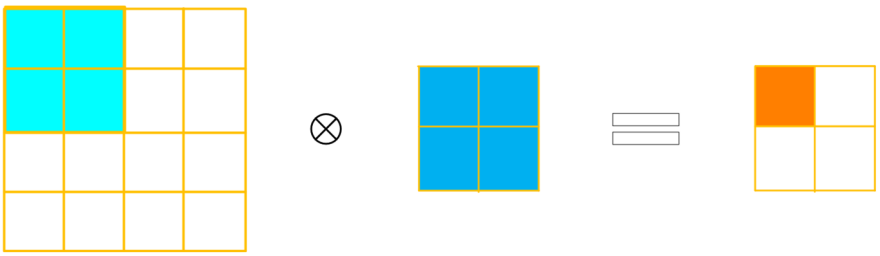

FIG. 1. Convolutional operation.

an input x, this process can be formulated as

$$x^l = f\left(\sum x^{l-1} * w^l + b^l\right), \tag{12}$$

where b and w are the bias and filter, respectively, and l denotes the layer number.

After computing the convolutional layer, a max-pooling layer is used to reduce the variability. Specifically, the max-pooling operation will receive activations from the previous convolutional layer and then output a maximum of a selected band, which indicates that the max-pooling layer is a sub-sampling process. The max-pooling process is given by

$$x^l = f(\beta^l \,\mathrm{down}(x^{l-1}) + b^l), \tag{13}$$

where x^{l-1} means the previous layer of convolution, down $(\cdot)$ denotes down sampling, and β is the scale.

When the network is used for prediction, a fully connected layer is needed. The output layer is the predicted value we expect, which can be formulated as

$$\hat{y} = f(W \cdot x + b), \tag{14}$$

where W is the weight that needs to be optimized.

Given the true values, if the L2 norm loss function is considered,[29] the error between the predicted values and true values can be expressed as

$$E = \frac{1}{2}\sum \|y_i - \hat{y}_i\|_2^2, \tag{15}$$

where y_i means the true value of the ith sample and $\hat{y}_i$ is the corresponding deep CNN-generated value.

In the optimization process, the backpropagation algorithm is used to calculate the derivatives and then stochastic gradient descent is used for the optimization of the parameters,

$$W = W - \eta\frac{\partial E}{\partial W}, \quad \frac{\partial E}{\partial W} = f'(\cdot) \odot (\hat{y} - y), \tag{16}$$

where $f'(\cdot)$ is the derivative of the activation function and $\odot$ denotes the element-wise multiplication.

In the present application, a seven-layered convolution neural network is used to directly map the image pixels of the repeating unit cells onto their corresponding thermo-mechanical moduli. The first representational layer $\boldsymbol{x}$ abstracts image pixels of a repeating unit cell at a given fiber content and distribution while the output layer identifies the homogenized thermo-mechanical moduli $\hat{y}$ of the considered RUC. A deep convolution network describes potentially causal connections between input and output properties through a nonlinear relationship.

III. RESULTS AND DISCUSSIONS

The construction of the CNN-driven homogenization technique is carried out in three steps. First, we consider graphite/epoxy and glass/epoxy composite material systems with continuous reinforcements whose response may be characterized by periodically repeating material microstructure with two-dimensional periodicity. The elastic moduli and thermal expansion coefficients of fiber and resin phases are listed in Table I. While the graphite fiber is transversely isotropic, glass fibers are isotropic with a greater in-plane elastic modulus contrast relative to the epoxy resin than in the case of graphite fibers, providing a vigorous and demanding test of the proposed surrogate model. For each material system, 40 000 RUC images containing an arbitrary number of locally irregular inclusions are generated in MATLAB using the "rand" function, hence covering a wide range of fiber volume fractions ranging from 0% to 100%. It should be noted that we limit our analysis to composites reinforced by continuous fibers with square cross-sectional shapes, Fig. 2(a). Modeling a large number of locally irregular circular fibers, which is beyond this paper's scope, may require a more sophisticated mesh discretization algorithm, and hence was not conducted. It is also important to note that the in-plane and out-of-plane homogenized properties of unidirectional graphite/epoxy and glass/epoxy composites with random fiber distributions are uncoupled with the effective stiffness matrix

TABLE I. Elastic moduli and thermal expansion coefficients of fiber and resin phases.

	E_A (GPa)	E_T (GPa)	G_A (GPa)	ν_A	ν_T	α_A (μ/K)	α_T (μ/K)
Glass fiber	80	80	33.33	0.2	0.2	4.73	4.73
Graphite fiber	214	14	28	0.2	0.25	−0.36	18
Resin	4.5	4.5	1.67	0.35	0.35	45	45

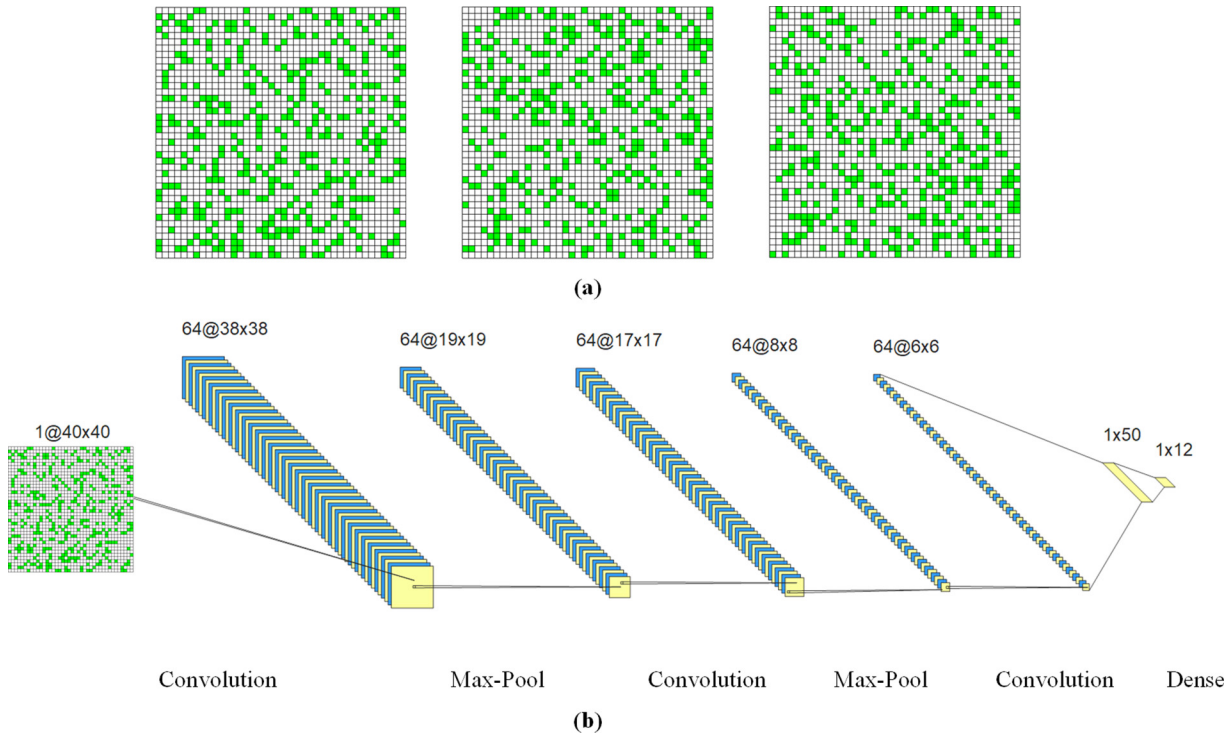

FIG. 2. (a) Illustration of three different repeating unit cells with locally irregular fibers containing 25% volume fractions. (b) Deep convolution neural network.

$\mathbf{C}^*$ expressed in the following form:

$$\mathbf{C}^* = \begin{bmatrix} C_{11}^* & C_{12}^* & C_{13}^* & C_{14}^* & 0 & 0 \\ C_{21}^* & C_{22}^* & C_{23}^* & C_{24}^* & 0 & 0 \\ C_{31}^* & C_{32}^* & C_{33}^* & C_{34}^* & 0 & 0 \\ C_{41}^* & C_{42}^* & C_{43}^* & C_{44}^* & 0 & 0 \\ 0 & 0 & 0 & 0 & C_{55}^* & C_{56}^* \\ 0 & 0 & 0 & 0 & C_{65}^* & C_{66}^* \end{bmatrix}. \tag{17}$$

Given that the unit cell as a whole comprises many randomly distributed fibers, its computed effective mechanical properties can be considered orthotropic or even transversely isotropic. The effective engineering moduli are obtained in terms of the effective compliance matrix $\mathbf{S}^* = [\mathbf{C}^*]^{-1}$,

$$\begin{aligned} &E_{11}^* = \frac{1}{S_{11}^*} \quad E_{22}^* = \frac{1}{S_{22}^*} \quad E_{33}^* = \frac{1}{S_{33}^*}, \\ &\nu_{12}^* = -E_{11}^* S_{21}^* \quad \nu_{13}^* = -E_{11}^* S_{31}^* \quad \nu_{23}^* = -E_{22}^* S_{32}^*, \\ &G_{23}^* = \frac{1}{S_{44}^*} \quad G_{13}^* = \frac{1}{S_{55}^*} \quad G_{12}^* = \frac{1}{S_{66}^*}. \end{aligned} \tag{18}$$

The homogenized properties E_{11}, E_{22}, E_{33}, G_{23}, G_{13}, G_{12}, ν_{12}, ν_{13}, ν_{23}, α_{11}, α_{22}, and α_{33} of each RUC (with the superscripts * omitted for simplification) are evaluated via the finite-volume homogenization technique.[30,31] The RUCs, in conjunction with the corresponding homogenized properties, are randomly split into two parts as the training dataset and testing dataset in a ratio of 90%:10%. Next, we construct a deep convolution neural network to associate the microstructural features of unit cells of periodic composites with their corresponding homogenized moduli. Since one layer of convolution is limited in feature extraction, it is necessary to set up a deep model to extract high-level features.[32,33] By stacking the layers together, the microstructural features can be extracted automatically. Figure 2(b) illustrates a seven-layered network employed in the present work, which includes the convolution layer, max-pooling layer, and dense layer. Third, the deep CNN model is trained using the randomly chosen training dataset, and subsequently, the test dataset is applied to the trained network to predict the homogenized properties of the remaining 4000 RUCs. It should be noted that the CNN model is trained just once for each material system. Once the network for a specified material system is obtained, the homogenized properties of a new RUC will be obtained upon securing an image of the material's microstructural features.

In the deep CNN model illustrated in Fig. 2, the input layer is the repeating unit cell of composite materials, which is represented by a 40×40 image matrix. The output layer comprises 12 independent homogenized thermo-mechanical properties of the composite E_{11}, E_{22}, E_{33}, G_{23}, G_{13}, G_{12}, ν_{12}, ν_{13}, ν_{23}, α_{11}, α_{22}, and α_{33}. It is worth noting that a deep learning process eliminates the need of

determining which microstructural features, such as statistical moments of fiber distributions at a given fiber content, fiber–fiber short-term and long-term distances, should be correlated with the homogenized moduli. Instead, the deep CNN disentangles these abstractions and picks out which features improve performance on its own. To reduce the dependence and redundancy of the data, the homogenized moduli generated by the finite-volume micromechanics are normalized using the following equation:

$$y_i = \frac{x_i - \min(\boldsymbol{x})}{\max(\boldsymbol{x}) - \min(\boldsymbol{x})}, \tag{19}$$

where $\boldsymbol{x} = (x_1, x_2, \ldots, x_i, \ldots, x_n)$, x_i are the homogenized Young's and shear moduli as well as the thermal expansion coefficients generated by the finite-volume micromechanics, $n = 40\,000$ indicates the number of RUCs, and y_i are the corresponding normalized moduli. To measure the errors generated during the training process, two metrics, namely, the mean absolute percentage error (MAPE) and mean percentage error (MPE), are defined as follows:

$$\text{MAPE} = \frac{100\%}{n}\sum_{i=1}^{n}\left|\frac{y_i - \hat{y}_i}{y_i}\right|, \tag{20}$$

$$\text{MPE} = \frac{100\%}{n}\sum_{i=1}^{n}\frac{y_i - \hat{y}_i}{y_i}, \tag{21}$$

where $\hat{y}_i$ are the CNN-generated homogenized moduli.

The training dataset was first used to train the convolution neural network. Figure 3 illustrates the loss value as a function of epoch generated during the training process for the graphite/epoxy

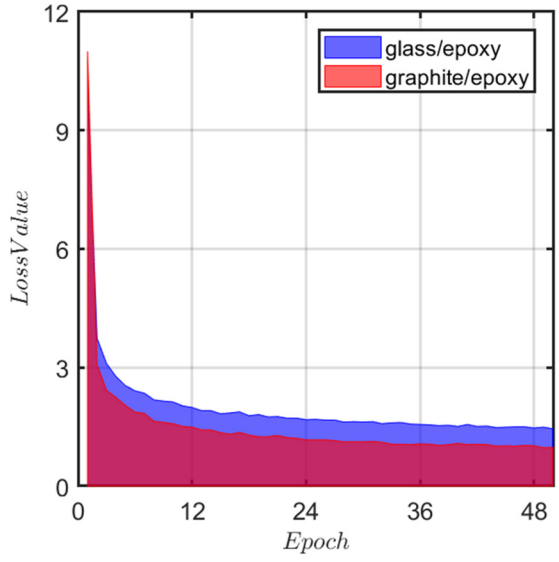

FIG. 3. Loss function generated during the training process.

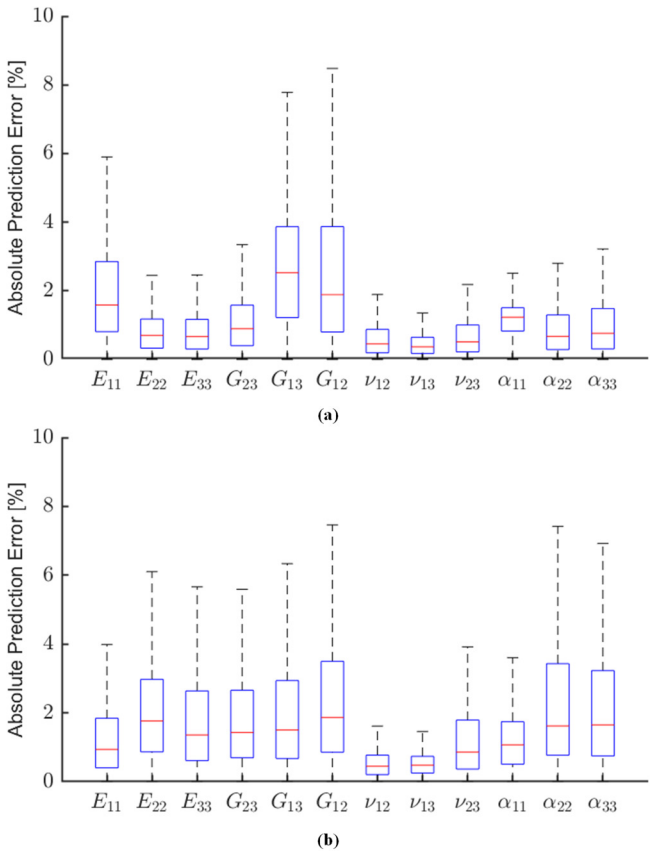

FIG. 4. Mean absolute prediction error generated during the test process: (a) graphite/epoxy composites; (b) glass/epoxy composites.

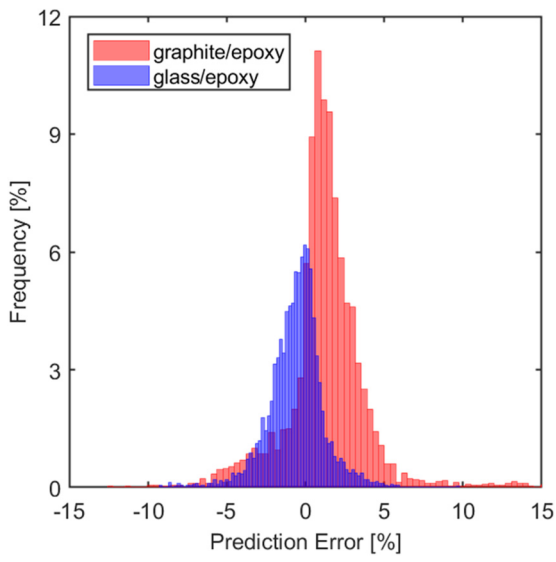

FIG. 5. Histogram of mean prediction error (%).

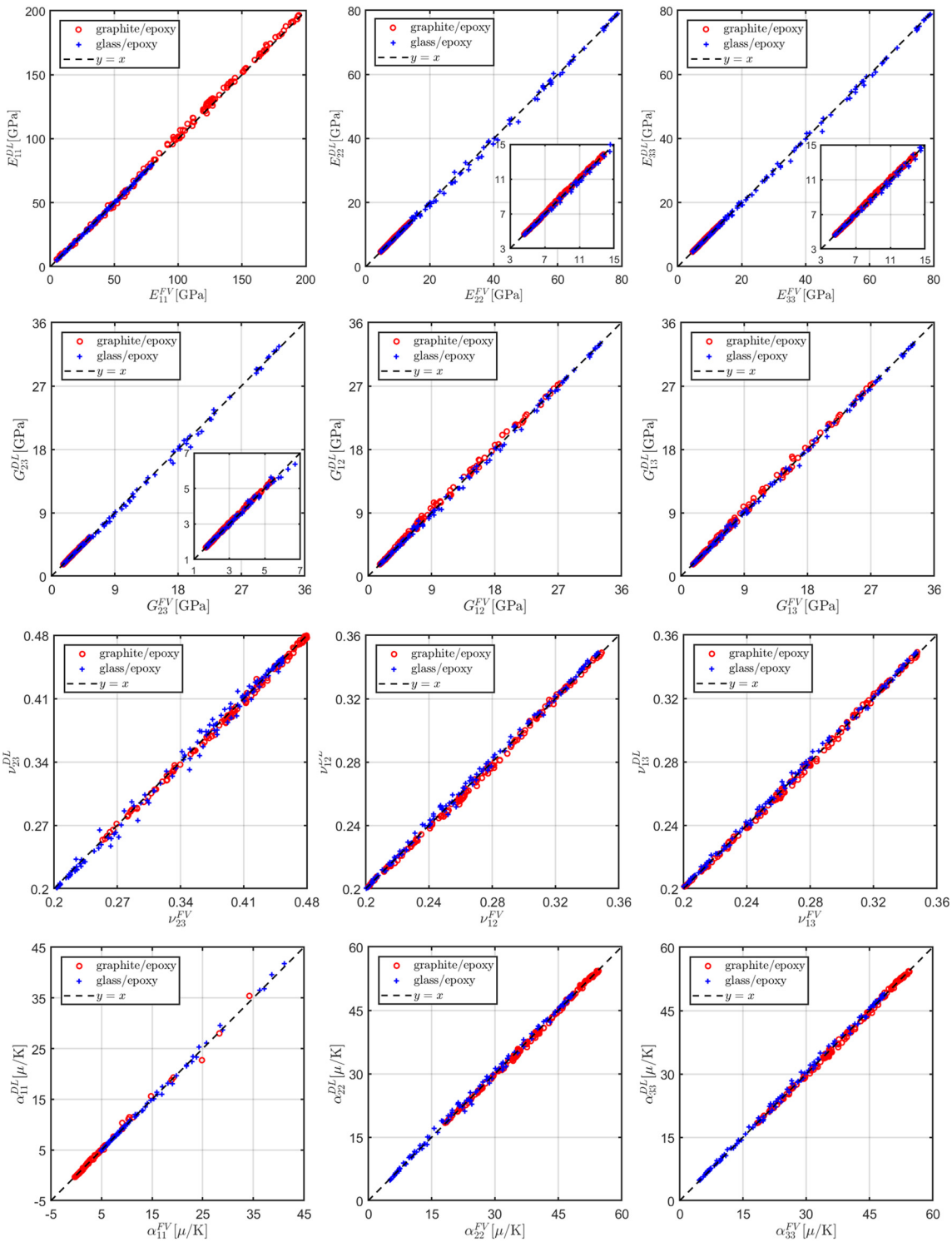

FIG. 6. Comparison of homogenized moduli predicted by the finite-volume micromechanics and CNN homogenization. The subscripts "FV" and "DL" represent the homogenized quantities generated by the finite-volume micromechanics and deep CNN model, respectively.

and glass/epoxy material systems. During the training process, the learning rate is set to be 0.06. After two epochs, the loss functions decrease to a value of 3 for both material systems. After 24 epochs, the loss functions converge to values smaller than 1.1 and 1.7 for the graphite/epoxy and glass/epoxy, respectively, and remain constant thereafter. It should be noted that only 195 s were used to execute the training program in an uncompiled python environment in virtue of the GPU computing on Intel (R) Xeon(R) Silver 4110 CPU@2.1 GHz, 64.0 GB memory, 64-bit Operating System.

The effectiveness of the deep CNN homogenization technique is verified by substituting the RUCs in the test dataset to the trained deep CNN model to predict their homogenized properties. Figures 4(a) and 4(b) present the box plot of the mean absolute percentage errors for the graphite/epoxy and glass/epoxy material systems, respectively, illustrating the five-number summary (maximum, minimum, median, first, and third quartile) of the errors generated for the test dataset. As observed, in all cases, the CNN-homogenized properties are obtained with an approximately maximum error of 8% relative to the finite-volume micromechanics-generated theoretical values, whereas the first and third quartiles fall within 1% and 4%, respectively, indicating the excellent predictive capability of the deep CNN model. We note that the mean absolute percentage errors are different between the 12 independent homogenized properties. For both material systems, smaller mean absolute percentage errors in the predicted Poisson's ratios ν_{12}, ν_{13}, and ν_{23} are observed than those of the remaining composite properties. This is attributed to the fact that the deep CNN used in the study is constructed for multi-task learning, which means that the network is capable of generating 12 estimates of the RUC homogenized properties in a single network. Poisson's ratios have a smaller dispersion than Young's and shear moduli and thermal expansion coefficients, hence they are less demanding. To better illustrate the distributions of prediction errors generated in the testing case, the histogram of the mean percentage error is shown in Fig. 5. Consistent with the previous observations, almost all CNN prediction errors fall within ±5% for both material systems.

Figure 6 compares the homogenized thermo-mechanical properties for both graphite/epoxy and glass/epoxy systems generated by the deep CNN against the targeted theoretical values obtained using the finite-volume micromechanics. For visualization purposes, the reference line $y = x$ is also enclosed in the figure. The horizontal coordinates are the finite-volume homogenization results while the vertical coordinates represent corresponding deep CNN predictions. All points are distributed in the vicinity of the reference line almost everywhere in the entire homogenized parameter range. This indicates that the CNN prediction coincides with the finite-volume homogenized properties, further demonstrating the excellent predictive capability of the proposed deep convolution neural network. It should be mentioned that the upper and lower bounds in the above figures correspond to the minimum and maximum fiber volume fractions only in the case of E_{11}, E_{22}, E_{33}, G_{23}, G_{13}, and G_{12}. The axial Poisson's ratios ν_{12} and ν_{13} and axial thermal expansion coefficient α_{11} decrease with increasing fiber content, whereas the in-plane Poisson's ratio ν_{23} and transverse thermal expansion coefficients α_{22} and α_{33} increase first and then decrease with increasing fiber content (not shown).

IV. CONCLUSIONS

A microstructural image-homogenized moduli correlation scheme is proposed for periodic composites with unidirectional reinforcement randomly distributed in the plane transverse to the reinforcement direction. A seven-layer deep convolution neural network is developed that is trained to associate the microstructural features of unit cells of periodic composites with their corresponding homogenized moduli, calculated using a finite-volume homogenization theory. The performances of the proposed network are assessed extensively by checking the loss value function during the training process, the five-number summary of the absolute mean prediction error, and mean percentage error distribution generated by the deep CNN homogenization. A direct comparison of the full set of homogenized properties by the deep CNN homogenization and finite-volume micromechanics theoretical values demonstrates excellent correlations between the data analysis and physical models. The full utility of the present approach may be realized upon incorporating the nonlinear analysis capabilities to generate the elastoplastic response, which will be reported elsewhere in our future work.

REFERENCES

[1]G. Wang and M.-J. Pindera, Mater. Des. **132**, 337 (2017).
[2]Z. He, G. Wang, and M.-J. Pindera, Compos. Struct. **222**, 110905 (2019).
[3]G. Wang, W. Tu, and M.-J. Pindera, Compos. Struct. **160**, 838 (2017).
[4]R. Christensen and K. Lo, J. Mech. Phys. Solids **27**, 315 (1979).
[5]M. Tane and T. Ichitsubo, Appl. Phys. Lett. **85**, 197 (2004).
[6]C. N. Della and D. Shu, Appl. Phys. Lett. **103**, 132905 (2013).
[7]G. Wang, W. Tu, and Q. Chen, Mech. Mater. **139**, 103178 (2019).
[8]M.-J. Pindera, H. Khatam, A. S. Drago, and Y. Bansal, Composites Part B **40**, 349 (2009).
[9]A. Drago and M.-J. Pindera, Compos. Sci. Technol. **67**, 1243 (2007).
[10]Z. Hashin, J. Appl. Mech. **46**, 543 (1979).
[11]T. Mori and K. Tanaka, Acta Metall. **21**, 571 (1973).
[12]R. Kar-Gupta, C. Marcheselli, and T. Venkatesh, J. Appl. Phys. **104**, 024105 (2008).
[13]R. Kar-Gupta and T. Venkatesh, J. Appl. Phys. **98**, 054102 (2005).
[14]A. S. Drago and M.-J. Pindera, J. Appl. Mech. **75**, 051010 (2008).
[15]M. Gattu, H. Khatam, A. S. Drago, and M.-J. Pindera, J. Eng. Mater. Technol. **130**, 031015 (2008).
[16]Q. Chen, G. Wang, and X. Chen, Int. J. Appl. Mech. **10**, 1850045 (2018).
[17]Q. Chen and M.-J. Pindera, Int. J. Plast. **124**, 42 (2020).
[18]Q. Chen, G. Wang, and M.-J. Pindera, Composites Part B **155**, 329 (2018).
[19]M. Reichstein, G. Camps-Valls, B. Stevens, M. Jung, J. Denzler, and N. Carvalhais, Nature **566**, 195 (2019).
[20]Y. Iwasaki, R. Sawada, V. Stanev, M. Ishida, A. Kirihara, Y. Omori, H. Someya, I. Takeuchi, E. Saitoh, and S. Yorozu, NPJ Comput. Mater. **5**, 1 (2019).
[21]D. Melati, Y. Grinberg, M. K. Dezfouli, S. Janz, P. Cheben, J. H. Schmid, A. Sánchez-Postigo, and D.-X. Xu, Nat. Commun. **10**, 4775 (2019).
[22]S. Ekins, A. C. Puhl, K. M. Zorn, T. R. Lane, D. P. Russo, J. J. Klein, A. J. Hickey, and A. M. Clark, Nat. Mater. **18**, 435 (2019).
[23]R. Collobert and J. Weston, *A Unified Architecture for Natural Language Processing: Deep Neural Networks with Multitask Learning* (ACM, 2008), p. 160.
[24]L. Deng and D. Yu, Found. Trends Signal Process. **7**, 197 (2013).
[25]M. Ma, C. Sun, X. Chen, X. Zhang, and R. Yan, IEEE Trans. Ind. Inform. **15**, 6415 (2019).
[26]N. Charalambakis, Appl. Mech. Rev. **63**, 030803 (2010).
[27]Y. LeCun, Y. Bengio, and G. Hinton, Nature **521**, 436 (2015).

[28]T. N. Sainath, A.-R. Mohamed, B. Kingsbury, and B. Ramabhadran, *Deep Convolutional Neural Networks for LVCSR* (IEEE, 2013), p. 8614.
[29]M. Ma and Z. Mao, *Deep Recurrent Convolutional Neural Network for Remaining Useful Life Prediction* (IEEE, 2019), p. 1.
[30]Q. Chen, G. Wang, and M.-J. Pindera, Eur. J. Mech. A Solids **70**, 141 (2018).
[31]M. A. Cavalcante, M.-J. Pindera, and H. Khatam, Composites Part B **43**, 2521 (2012).
[32]Z. Chen, K. Gryllias, and W. Li, Mech Syst Signal Pr **133**, 106272 (2019).
[33]M. Ma, C. Sun, and X. Chen, IEEE Trans. Instrum. Meas. **66**, 3115 (2017).